

Highly sensitive size discrimination of sub-micron objects using optical Fourier processing based on two-dimensional Gabor filters

Robert M. Pasternack,¹ Zhen Qian², Jing-Yi Zheng,¹ Dimitris N. Metaxas³, and Nada N. Boustany^{1*}

¹Department of Biomedical Engineering, Rutgers University, Piscataway, New Jersey 08854, USA

²Piedmont Heart Institute, Piedmont Hospital, Atlanta, Georgia 30309, USA

³Department of Computer Science, Rutgers University, Piscataway, New Jersey 08854, USA

*nboustan@rci.rutgers.edu

Abstract: We use optical Gabor-like filtering implemented with a digital micromirror device to achieve nanoscale sensitivity to changes in the size of finite and periodic objects imaged at low resolution. The method consists of applying an optical Fourier filter bank consisting of Gabor-like filters of varying periods and extracting the optimum filter period that maximizes the filtered object signal. Using this optimum filter period as a measure of object size, we show sensitivity to a 7.5 nm change in the period of a chirped phase mask with period around 1 μ m. We also show 30nm sensitivity to change in the size of polystyrene spheres with diameters around 500nm. Unlike digital post-processing our optical processing method retains its sensitivity when implemented at low magnification in undersampled images. Furthermore, the optimum Gabor filter period found experimentally is linearly related to sphere diameter over the range 0.46 μ m–1 μ m and does not rely on a predictive scatter model such as Mie theory. The technique may have applications in high throughput optical analysis of subcellular morphology to study organelle function in living cells.

©2009 Optical Society of America

OCIS codes: (070.6110) Spatial Filtering, (070.1170), Analog optical signal processing, (120.5820) Scattering measurements, (180.0180) Microscopy.

References and links

1. Z. Pincus, and J. A. Theriot, "Comparison of quantitative methods for cell-shape analysis," *J. Microsc.* **227**(2), 140–156 (2007).
2. J. Angulo, and S. Matou, "Application of mathematical morphology to the quantification of in vitro endothelial cell organization into tubular-like structures," *Cell Mol Biol (Noisy-le-grand)* **53**(2), 22–35 (2007).
3. A. Heifetz, J. J. Simpson, S.-C. Kong, A. Taflove, and V. Backman, "Subdiffraction optical resolution of a gold nanosphere located within the nanojet of a Mie-resonant dielectric microsphere," *Opt. Express* **15**(25), 17334–17342 (2007).
4. J. D. Wilson, and T. H. Foster, "Mie theory interpretations of light scattering from intact cells," *Opt. Lett.* **30**(18), 2242–2244 (2005).
5. Y. L. Kim, Y. Liu, R. K. Wali, H. K. Roy, M. J. Goldberg, A. K. Kromin, K. Chen, and V. Backman, "Simultaneous Measurement of Angular and Spectral Properties of Light Scattering for Characterization of Tissue Microarchitecture and its Alteration in Early Precancer," *IEEE J. Sel. Top. Quantum Electron.* **9**(2), 243–256 (2003).
6. H. Fang, M. Ollero, E. Vitkin, L. M. Kimerer, P. B. Cipolloni, M. M. Zaman, S. D. Freedman, I. J. Bigio, I. Itzkan, E. B. Hanlon, and L. T. Perelman, "Noninvasive sizing of subcellular organelles with light scattering spectroscopy," *IEEE J. Sel. Top. Quantum Electron.* **9**(2), 267–276 (2003).
7. J. R. Mourant, T. M. Johnson, S. Carpenter, A. Guerra, T. Aida, and J. P. Freyer, "Polarized angular dependent spectroscopy of epithelial cells and epithelial cell nuclei to determine the size scale of scattering structures," *J. Biomed. Opt.* **7**(3), 378–387 (2002).
8. J. D. Wilson, C. E. Bigelow, D. J. Calkins, and T. H. Foster, "Light scattering from intact cells reports oxidative-stress-induced mitochondrial swelling," *Biophys. J.* **88**(4), 2929–2938 (2005).
9. L. Xu, A. Taflove, and V. Backman, "Recent progress in exact and reduced-order modeling of light scatter properties of complex structures," *IEEE J. Sel. Top. Quantum Electron.* **11**(4), 759–765 (2005).

10. R. M. Pasternack, Z. Qian, J.-Y. Zheng, D. N. Metaxas, E. White, and N. N. Boustany, "Measurement of subcellular texture by optical Gabor-like filtering with a digital micromirror device," *Opt. Lett.* **33**(19), 2209–2211 (2008).
 11. I. Fogel, and D. Sagi, "Gabor filters as texture discriminator," *Biol. Cybern.* **61**(2), 103–113 (1989).
 12. R. Mehrotra, K. R. Namuduri, and N. Ranganathan, "Gabor filter-based edge detection," *Pattern Recognit.* **25**(12), 1479–1494 (1992).
 13. J. G. Daugman, "Uncertainty relation for resolution in space, spatial frequency, and orientation optimized by two-dimensional visual cortical filters," *J. Opt. Soc. Am. A* **2**(7), 1160–1169 (1985).
 14. N. N. Boustany, S. C. Kuo, and N. V. Thakor, "Optical scatter imaging: subcellular morphometry in situ with Fourier filtering," *Opt. Lett.* **26**(14), 1063–1065 (2001).
-

1. Introduction

Quantitative measurement of subcellular structure and dynamics is important for more rigorous morphological description of biological cells and hence for better understanding of their structure-function relationships. Cell dynamics in processes such as cell death, cell differentiation and cell division show space and time dependent qualities with morphological changes controlled by intrinsic molecular pathways within the cell. Quantification of these morphological changes is critical in gaining a more complete understanding of cellular function. Currently, direct imaging to quantify cell morphology in situ requires high resolution fluorescence, and a comparatively low-throughput analysis. Very high sensitivity but very low throughput analysis is possible using electron microscopy, but this technique is limited as it requires sample sectioning and fixation and therefore cannot be used to track dynamic structural alterations.

In addition to fluorescence methods, several innovative optical techniques have been developed to optically probe samples with complex morphologies. Recent efforts have been made to develop quantitative descriptors for cell shape, size and other morphological parameters gleaned from optical microscopic imaging [1], and computational image analysis has aided considerably in this effort [2]. Scattering and spectroscopic detection methods continue to prove extremely useful in measuring spherical particle size with accuracy even beyond the diffraction limit using Mie theory [3,4]. Other approaches use the light scatter spectra as a metric that can be correlated to different sample states (e.g. normal vs. diseased in a tissue sample [5]). Light scattering is used in scanning microscopy with modeling to extract particle size and shape based on spectra collected at each point [6]. Angular scattering spectroscopy has also been successfully applied to living cells to measure subcellular organelles [7] and mitochondrial swelling [8]. In parallel, progress is also being made in modeling of light scatter through complex structures [9].

In Pasternack et al. [10] we showed the use of a digital micromirror device (DMD) as a spatial light modulator capable of optical Fourier filtering of biological structures as a proof of principle for rapid-throughput quantitative morphological analysis. Although generally used in digital post-processing [11,12], we implemented two-dimensional (2D) Gabor filters [13] on the DMD making morphological measurements that can be encoded directly into an image. This technique demonstrated the ability to detect subcellular texture parameters such as orientation and aspect ratio of organelles [10]. We now more thoroughly explore the implementation of Gabor-like filters using the DMD as an optical Fourier filter by demonstrating its sensitivity to changes in the dimension of periodic and finite objects of known period and size, and we discuss this technique's usefulness in situations where digital filtering may prove inadequate. Moreover, we show that the Gabor filter method returns a lengthscale on the order of the object's structure that can be directly measured experimentally and does not depend on inference from a predictive theoretical scattering description such as Mie theory.

2. Methods

2.1 Optical Setup and Image Acquisition

The optical Fourier processing microscope was initially described in Pasternack et al. [10]. For Fourier filtering, we placed a Digital Micromirror Device (DMD) (TI 0.7 XGA DMD, by

Texas Instruments) in a conjugate Fourier plane of an inverted commercial microscope (Axiovert 200M, Zeiss, Göttingen Germany) fitted with a 20x NA = 0.75 objective. Light from a ~5 mW Helium-Neon laser ($\lambda_0 = 632.8$ nm) is passed through a spinning diffuser and coupled into a multimode fiber whose output is collimated and launched into the microscope's condenser aligned in central Köhler illumination (NA<0.05). Image acquisition consisted of collecting on a 16-bit CCD (Roper Scientific Cascade 512B) a stack of spatially filtered dark-field images using a spatial filter bank generated by the DMD.

The DMD itself is a 1024x768 array of individually addressable $13.7 \times 13.7 \mu\text{m}^2$ mirrors, which can be programmed to deflect the light towards or away from the CCD detector, thus allowing for binary on/off amplitude modulation of the field at each mirror. To analyze feature size for objects within the resolution of the microscope system, we programmed the DMD to display a set of two dimensional (2D) Gabor-like filters with varying period. As in [10], we approximated the Gabor filter by generating four concentric binary discs (Fig. 1). These filters are applied to the DMD so that the DMD cycles through each of its layers every ~5 ms during a 250-2000 ms exposure (depending on application) thereby automatically summing the filtered images associated with the four concentric discs during signal acquisition. Also as in [10], the current summation of the four concentric discs is not a coherent summation. However, because the discs are centered at the same position in the Fourier plane, the phase component of each associated filtered image is not significantly altered, thereby allowing for the approximation of each Gabor-filtered image simply by summing the four filtered images with equal exposure time.

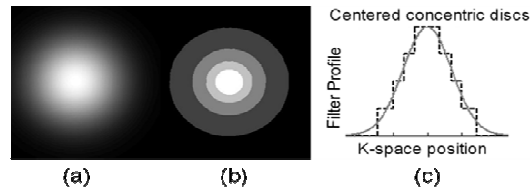


Fig. 1. Illustration of DMD implementation of Gabor filter. (a): Ideal Gabor Filter in k-space. (b): DMD approximation formed by overlay of binary concentric discs. (c): Overlapping profile views of (a) and (b).

Calibration of the Fourier plane is accomplished with a graticule with line spacing $a = 10 \mu\text{m}$. For diffraction order n at angle θ with respect to the optical axis, spatial frequency (in cycles/ μm) was defined as $\sin\theta/\lambda_0 = n/a$. Positions of the orders of the grid in the Fourier plane are measured in mirrors from the zeroth order position (DC component) with the aid of a DMD mirror ruler which is simply a filter with passbands at regular intervals. The calibration gave on average 12.80 mirrors per order, giving 0.00781 cycles/ μm /mirror. The maximum aperture (NA = 0.75) for the 20X objective corresponds to 1.185 cycles/ μm or a radius of 152 DMD mirrors.

2.2 Sample preparation

Two periodic phase masks were studied as suitable narrowband test objects: the first, an unchirped phase mask with period $1.075 \mu\text{m}$ (frequency 0.930 cycles/ μm), and the second, a chirped phase mask with chirp rate of 7.5 nm/mm around a nominal period of $1.05 \mu\text{m}$. The masks were translated along the periodic direction and data were collected at several points of 1 mm (chirped) or 2 mm (unchirped) intervals with arbitrary independent starting points x_0 .

To test the sensitivity to changes in finite object size, polystyrene microspheres (Polysciences, Inc, diluted in deionized water 10x.) were fixed in acrylamide gel (3:2:2:16 mix of sphere solution, 1% ammonium persulfate (Bio-Rad) in deionized water, 1% tetramethylethylenediamine (Bio-Rad) in deionized water, and acrylamide pre-mix (Bio-Rad)) to yield approximately 500-1000 spheres per $140 \mu\text{m} \times 140 \mu\text{m}$ field. The gel thickness on the coverslip is approximately $5 \mu\text{m}$, implying that spheres will appear in many focal planes. Six samples containing 465 nm, 494 nm, 548 nm, 771 nm, 989 nm or 1053 nm diameter spheres were prepared in this manner.

2.3 Analysis of the Optically Filtered Images

A Gabor filter is a linear filter defined by the product of a Gaussian envelope and a complex sinusoidal carrier in the object space [13]. In Fourier space our Gabor impulse response is:

$$H(u, v) = A_1 e^{-2\pi^2 \sigma_s^2 [(u-U_h)^2 + (v-V_h)^2]} \quad (1)$$

with amplitude A_1 and center located at frequencies (U_h, V_h) in cycles/ μm . In the object space, the period and orientation of the sinusoid are

$$S = \frac{1}{\sqrt{U_h^2 + V_h^2}}, \text{ and } \varphi = \arctan(V_h / U_h) \quad (2, 3)$$

respectively, and the extent of the Gaussian envelope is σ_s . The filters are scaled such that the amplitude of the filter in the frequency domain remains constant. The Gabor filter response at each position in the object is given by the convolution of the Gabor filter with the object, and is directly obtained in our system by applying the Gabor-like filter (Fig. 1) on the DMD while collecting the image of the object on the CCD camera. To analyze all possible feature sizes that may be present in the object, a Gabor filter bank consisting of many individual Gabor filters with incrementally changing values of S is applied to the object. The size of the local object feature present at a given pixel in the resulting Gabor filtered images is analyzed by measuring the pixel response as a function of Gabor filter period. The Gabor filter period that maximizes the pixel response is then taken as a measure of the local feature size. The localization of the Gabor filter response in object space depends on the extent of the Gabor filter Gaussian envelope, σ_s .

In our experiments we collected Gabor filter responses as a function of S by collecting two stacks of filtered images, each using a different filter bank for the periodic phase masks and sphere samples, respectively. Figure 2 illustrates the image acquisition and analysis sequence. First, a filter bank of four-layer Gabor-like filters with increasing center frequency and arrayed radially in the Fourier plane are constructed as illustrated in Fig. 2(a) and applied sequentially on the DMD while imaging the object; the resulting stack of filtered images (Fig. 2(b)) encode the pixel-by-pixel amplitude response as a function of applied Gabor filter frequency. After normalizing to exposure time, these data (squares in Fig. 2(c)) are then fit using non-linear least-squares Gaussian fitting (solid line in Fig. 2(c)), yielding the optimum Gabor frequency giving maximum response at each pixel. The optimum Gabor frequency is converted to optimum Gabor period, S_{max} . The data are encoded into color-coded images indicating optimum Gabor frequency (or period) vs. pixel (Fig. 2(d)). At each pixel, the value of S_{max} was then taken as a measure of local phase mask period or sphere diameter.

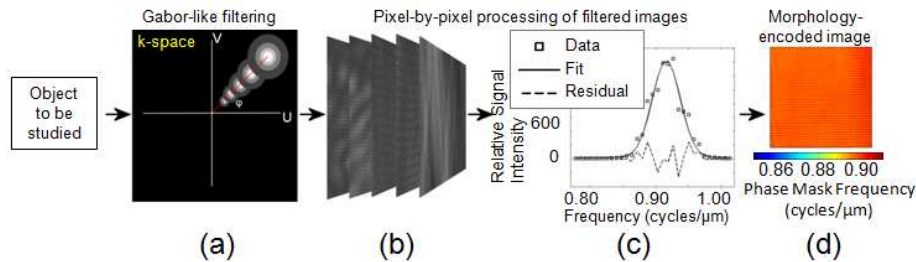


Fig. 2. Illustration of DMD implementation of Gabor filter bank and subsequent processing shown here for a phase mask data set. (a): Gabor-like filter bank applied to optical object transform in k-space. (b): Resultant stack of Gabor-like filtered images. (c): Representative fit of filter response as a function of Gabor filter frequency at one pixel of the image stack. Squares represent data points, the solid line represents the fit, and the dashed line represents the residual. (d): Morphometric-encoded image generated from fit for all pixels in the image. The colorscale indicates the Gaussian mean resulting from the pixel response fit and thus gives at each pixel the optimum Gabor filter frequency, $1/S_{\text{max}}$, giving maximum response.

2.4 Digital Processing of Phase Mask Images

We compared our optical filtering method with digital post-processing of images of the phase masks collected in bright field microscopy. Unfiltered bright field (BF) images of the chirped and unchirped phase masks were acquired at high magnification (0.080 $\mu\text{m}/\text{pixel}$) and low magnification (0.205 $\mu\text{m}/\text{pixel}$) without aliasing (Figs. 3(a) and 3(b), respectively). The masks were measured at several points of 1 mm (chirped) or 2 mm (unchirped) intervals as described above. The images were post-processed digitally using Gabor filters with $\sigma_s = S$ applied in image space. The period of the phase mask was measured at each pixel by optimizing the period of the Gabor filter to give maximum image pixel response. The optimization algorithm utilized an unconstrained nonlinear minimization (Nelder-Mead Simplex Method).

2.5 Digital Processing of Sphere Images

We also digitally analyzed dark-field (DF) and differential interference contrast (DIC) images of the fields of view used to study the 465nm, 494nm and 548nm sphere samples by optical processing. The images were Fourier-transformed digitally and filtered using a digital Gabor filter bank. This generates a set of filtered image transforms which are then reverse-transformed and processed pixel-by-pixel as was done for optical processing.

Since the spheres are not periodic objects, the sphere images were also digitally post-processed using a non-Gabor based digital processing method. In this procedure, a template-matching algorithm was used to first detect the spheres in the DIC and dark-field images. The template was designed as the second derivative of a symmetric 2D Gaussian simulated as the difference of two 2D Gaussians:

$$F = N(t_x, t_y, \sigma) - N(t_x, t_y, 2\sigma) \quad (4)$$

where (t_x, t_y) is the 2D translation, and σ and 2σ are the standard deviations of the two Gaussians, respectively. Then, at each of the spheres, the local sphere image was convolved with the 2D template, and the sphere size was measured by optimizing the 2D translation and the standard deviation of the 2D template. The optimized σ gave a relative measurement of the sphere size, which was converted to sphere size using the known magnification of the image in number of pixels per micron. This optimization algorithm also utilized an unconstrained nonlinear minimization (Nelder-Mead Simplex Method).

3. Results

3.1 Optical Processing of Periodic Phase Masks

For reference, bright field (BF) images of the chirped periodic phase mask are shown in Fig. 3 using a 0.080 $\mu\text{m}/\text{pixel}$ or 0.205 $\mu\text{m}/\text{pixel}$ magnification (Figs. 3(a) and 3(b)). The image magnification was achieved by selecting the focal distance of an imaging lens placed in front of the CCD without changing the 20X objective or the 0.75 numerical aperture of the system at the level of the DMD. A filter bank of 57 four-layer Gabor-like filters ranging in center frequency from 0.734 cycles/ μm to 1.172 cycles/ μm in one mirror increments (0.00781 cycles/ μm increment) and arrayed in the Fourier plane 90° from the orientation of the phase mask lines were constructed; the entire Fourier plane frequency range was not used in the expectation that the signal energy from the periodic object will be localized to a frequency near 0.93 cycles/ μm as indicated by the manufacturer. The extent of the Gabor filter was set to $\sigma_s = S$. The image magnification for optical Gabor filtering was 0.275 $\mu\text{m}/\text{pixel}$. The Gabor-filtered phase mask images are essentially featureless (Fig. 3(c)) due to the absence of the Gabor complex conjugate; however, the Gabor filtering results in images that are spatially confined as indicated by the preservation of the condenser field stop boundary. All images taken contain signal significantly above background levels due to the width of the Gabor filters; however, signal strength is maximized when the Gabor filter is centered over the diffraction order and decreases as the filter position is moved away. The pixel-by-pixel amplitude response as a function of applied Gabor filter frequency was fit using non-linear

least-squares Gaussian fitting as explained previously (Fig. 2(c)), and encoded into color-coded images indicating mask order frequency vs. pixel (Fig. 4(a)). The Gaussian fit to the Gabor response at each pixel produced a correlation of greater than 80% in >99% of pixels. Analysis of the encoded images of the chirped phase mask produced a mask period vs. stage position relationship (Fig. 4(b)) in which the chirp mask period is linearly decreasing with relative position at a rate of 7.6nm/mm (correlation = 0.98), 0.1 nm/mm higher than the provided manufacturer specifications but well within the error of the optical setup. Analysis of the encoded images for the unchirped phase mask produced a nearly constant period ranging from 1.074 +/- 0.002 to 1.077 +/-0.003 μm , and within 3 nm of the 1.075 μm period specified by the manufacturer (Fig. 4(b), gray squares).

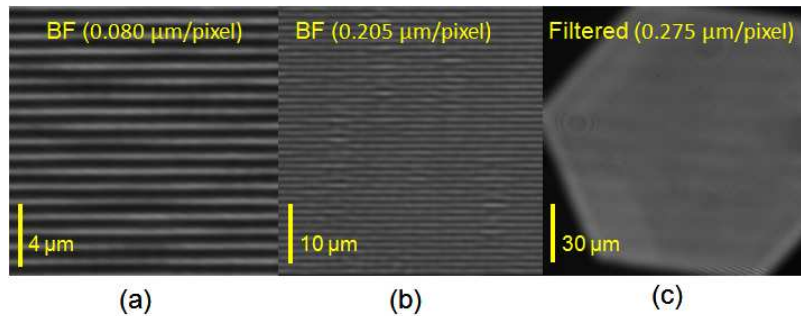


Fig. 3. Representative phase mask images. (a) Bright field taken at 0.080 $\mu\text{m}/\text{pixel}$, (b): Bright field taken at 0.205 $\mu\text{m}/\text{pixel}$ (c): Gabor-filtered image filtered at mask frequency, showing the edge of the condenser field stop and taken at 0.275 $\mu\text{m}/\text{pixel}$. Optically filtered images were used for optical processing. Bright field images were used for digital post-processing (Section 3.2).

3.2 Digital Gabor processing of Periodic Phase Masks

For digital post-processing, unfiltered phase mask images were acquired through the setup by passing all mirrors of the DMD. All images are taken in bright field in this case to yield non-aliased images at the CCD at 0.080 $\mu\text{m}/\text{pixel}$ and 0.205 $\mu\text{m}/\text{pixel}$ magnification (Figs. 3(a) and 3(b)). Figure 4(c) illustrates the results of digital Gabor filtering obtained by digital post-processing of the phase mask bright field images. When imaged at 0.080 $\mu\text{m}/\text{pixel}$, digital Gabor filtering measures the period to be linearly decreasing with position with a nominal chirp rate of 7.5 nm/mm based on a linear fit, exactly the expected value specified by the manufacturer (Fig. 4(c), gray line). However, when imaged at 0.205 $\mu\text{m}/\text{pixel}$ (Fig. 4(c), black line), a linear fit of the digital Gabor filtering measures a nominal chirp rate of 6.5 nm/mm, significantly lower than the expected value by 1.0 nm/mm, and the measured periods range from 0.75 to 0.79 μm , much lower than the high magnification measurement in the same vicinity of the phase mask. Additionally, the period is no longer observed to be monotonically decreasing with incremental movements of the stage. At points 3 and 5, the value of the measured mask period increases from its previous value at the prior position, yielding a positive chirp rate for these two positions. Finally, the error of the measurement is much greater in value at several points than the errors for either high-magnification digital processing (Fig. 4(c) gray line) or optical processing (Fig. 4(b)), demonstrating that high magnification is necessary for both precision and accuracy of digital post-processing.

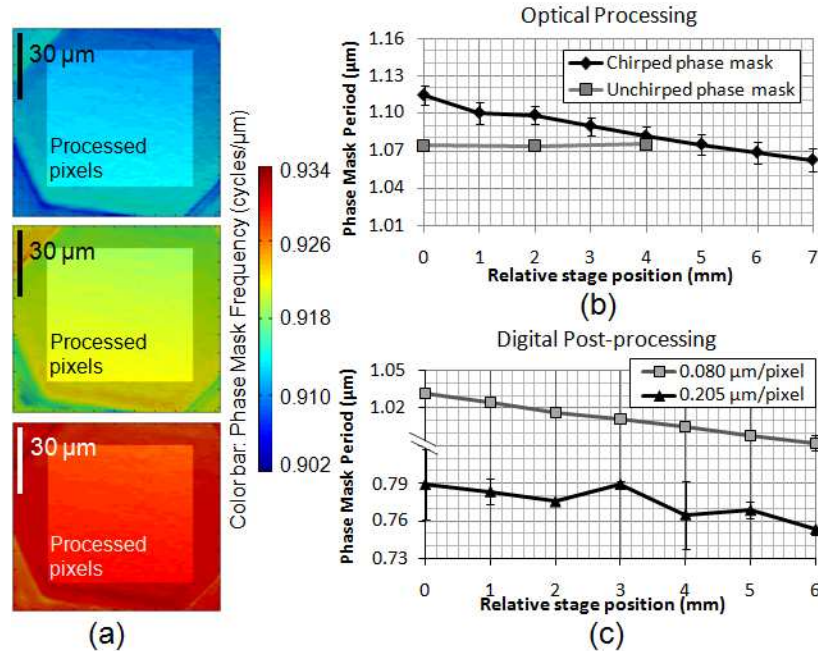


Fig. 4. Optical and digital Gabor filtering of phase masks. (a): Top to bottom: Color-coded images encoding measured phase mask frequency pixel-by-pixel from optical Gabor-like filtering at locations 1 mm, 3mm and 5mm from arbitrary starting point $x_0 = 0$ on chirped phase mask. Darkened regions of each image are excluded from analysis (b): Measured chirp as a function of displacement along the chirped (black diamonds) and unchirped (gray squares) phase masks imaged at $0.275 \mu\text{m}/\text{pixel}$ using Gabor-like optical filtering. Data are mean \pm standard deviation of the pixel values included in the processed regions of interest (ROI) (e.g. highlighted regions within the color encoded images in panel (a)). (c): Measured chirp as a function of displacement along the chirped phase mask imaged in bright field at $0.205 \mu\text{m}/\text{pixel}$ (black triangles) and $0.080 \mu\text{m}/\text{pixel}$ (gray squares) and digitally post-processed using Gabor digital filtering. Data are mean \pm standard deviation of the mask periods measured at the pixels included in the processed ROI's within the bright field images. The analyzed ROI's were pixel rows 80-446 and columns 65-446 for optical processing (highlighted areas in (a)), and pixel rows 75-448 and columns 75-448 for digital post-processing.

3.3 Optical Processing of Sphere Samples

Representative images of the spheres in dark-field (DF) and differential interference contrast (DIC) are shown in Fig. 5. The magnification was $0.275 \mu\text{m}/\text{pixel}$. The same general scheme as outlined in Fig. 2 is once again used. A Gabor filter bank with filters centered on mirrors 50 (corresponding to $0.391 \text{ cycles}/\mu\text{m}$) to 150 (corresponding to $1.172 \text{ cycles}/\mu\text{m}$) was applied to the DMD to examine the 465 nm, 494 nm, 548 nm sphere samples while a Gabor filter bank with filters centered on mirrors 20 (corresponding to $0.156 \text{ cycles}/\mu\text{m}$) to 150 (corresponding to $1.172 \text{ cycles}/\mu\text{m}$) was applied to the DMD to examine the 771 nm, 989 nm, and 1053 nm sphere samples. The frequency increment was one mirror ($0.00781 \text{ cycles}/\mu\text{m}$ increment), $\phi = 0^\circ$, and $\sigma_s = S/2$. Each resulting set of optically filtered images (Figs. 5(c) and 5(h)) was analyzed pixel-by-pixel using the Gaussian fitting scheme previously described, and an encoded image of optimum Gabor period, S_{max} , (Figs. 5(d) and 5(i)) was produced for each sample. This image was then scaled to the dark field intensity image (Figs. 5(e) and 5(j)).

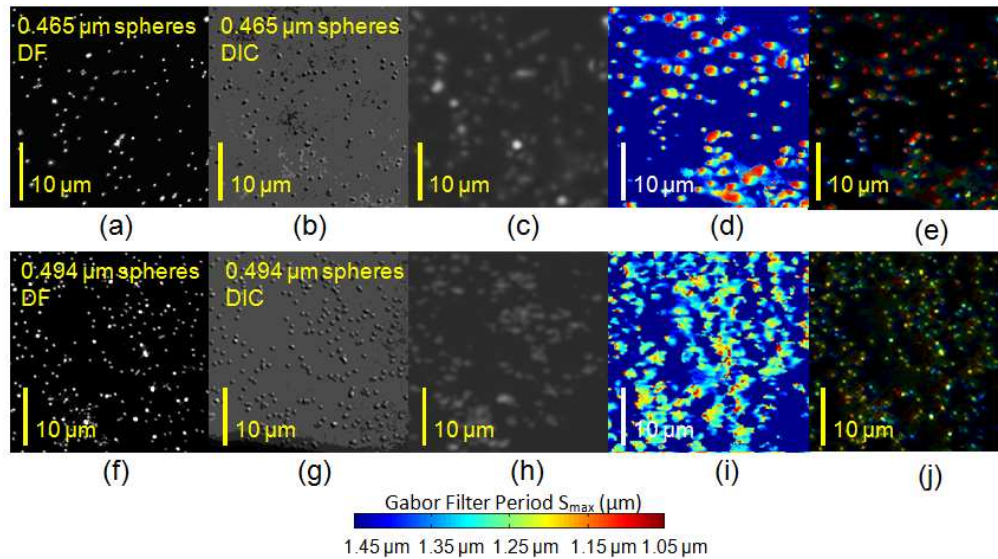


Fig. 5. Optical processing of 0.465 μm (top row) and 0.494 μm (bottom row) polystyrene microspheres at low magnification (0.275 $\mu\text{m}/\text{pixel}$). (a): Representative dark field (DF) image of 0.465 μm spheres in polyacrylamide gel. (b): Differential Interference Contrast (DIC) image. (c): Representative Gabor-filtered image. (d): Optically processed image encoding optimum Gabor period S_{max} giving maximal filter response. (e): Processed image encoding S_{max} gated to DF intensity image from Panel (a). (f) – (j): Same representation for 0.494 μm spheres in polyacrylamide gel as (a) – (e), respectively. For Panels (d) – (e) and (i) – (j), color hue encodes filter period S_{max} at which the filter response is maximized and intensity encodes relative fit amplitude.

Sample Gaussian fits to the optical response at one pixel for each sphere size tested are shown in Fig. 6(a). Each dark field-gated encoded image was thresholded by intensity to include points that are at least 12% of maximum intensity, thereby excluding the background but retaining other features. On the remaining pixels that were included which correspond to the locations where features are present, the Gaussian fitting correlation was greater than 80% in >95% of these pixels. These pixels were then analyzed to yield a per-feature (as opposed to per-pixel) data set encoding the average optimum Gabor period, S_{max} , for each feature finally yielding a per-feature histogram depicting the relative number of features (spheres) at each value of S_{max} for all three sphere samples (Fig. 6(b)). The statistics of these distributions are given in Table 1. For the spheres with diameter around 500nm, p values are shown for the comparison to the 494nm sphere size; for the 989nm spheres, the p value is shown for the comparison to the 1053nm sphere size. The differences between each sphere size are clearly observable. The distributions are tighter for the larger sphere sizes within the $\sim 0.5\mu\text{m}$ range, and the standard deviations of the measurements for the 0.494 μm and 0.548 μm sphere sizes are within the manufacturer's specifications (Fig. 6(b), Table 1). The relationship between Gabor period S_{max} and sphere size is plotted in Fig. 6(c) and follows a linear fit with the intercept pegged to zero (correlation coefficient = 0.99).

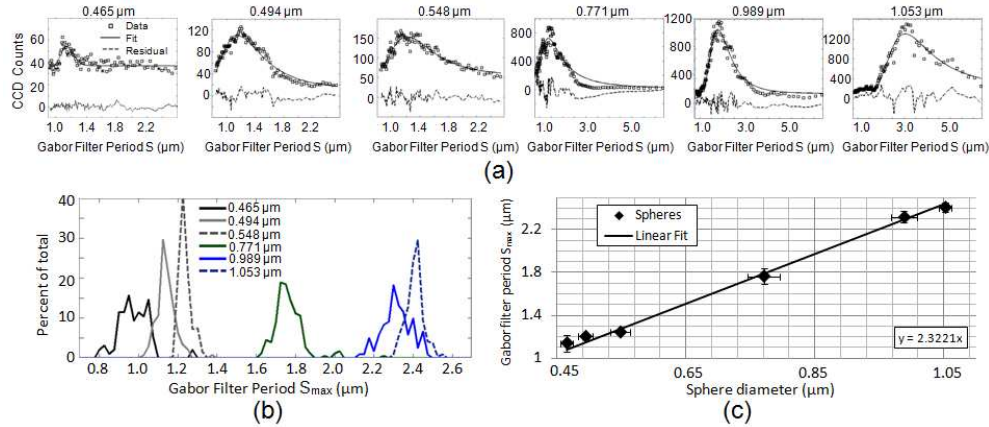


Fig. 6. Measurement of sphere size derived from optical Gabor-like processing. (a): Representative Gaussian fit to the filter response curve as a function of Gabor filter period at one pixel for (left to right) 0.465 μm , 0.494 μm , 0.548 μm , 0.771 μm , 0.989 μm and 1.053 μm sphere diameters. Fits are generated in the frequency domain before the abscissa is converted to Period. The fitted Gaussian mean gives the optimum period S_{max} that maximizes the filtered response. (b): Histogram showing the distribution of Gabor filter periods S_{max} at which local response for each sphere is maximized. Each sphere region is derived from the dark-field-gated responses (e.g. Fig. 5(e)). (c): Linear fit (with intercept fixed at zero) to plot of S_{max} as a function of sphere diameter. Data are the mean \pm standard deviation values found in Table 1. The coefficient of correlation between S_{max} and sphere diameter is 0.99.

Table 1. Optical filtering response showing nanoscale sensitivity to spheres with diameter ~ 500 nm

Actual diameter (nm) *	Gabor filter period S_{max} (nm) *	Student t-test p value
465 \pm 10	1140 \pm 78	$p < 0.08^\dagger$
494 \pm 11	1202 \pm 22	
548 \pm 16	1242 \pm 12	$p < 0.04^\dagger$
771 \pm 25	1765 \pm 75	
989 \pm 20	2317 \pm 54	$p < 0.03^\ddagger$
1053 \pm 10	2408 \pm 43	

* mean \pm standard deviation, † p value for comparison to 494nm, ‡ p value for comparison to 1053 nm

3.4 Digital post-processing of the Sphere Images

Dark-field (DF) and DIC images of the sphere samples collected at 0.275 $\mu\text{m}/\text{pixel}$ were Fourier-transformed digitally and filtered using a digital Gabor filter bank with center frequencies ranging from 67 to 206 pixels in radius on the Fourier plane (corresponding to a range of 0.475-1.463 cycles/ μm with frequency increment 0.00710 cycles/ μm) and with $\sigma_s = S/2$. For the DIC images, the orientation of the filter bank was parallel or perpendicular to the direction of maximal contrast. The generated filtered image transforms were then reverse-transformed and fit to a Gaussian pixel-by-pixel as was done for optical processing. After registration, the same pixels from the analog feature analysis are used in the digital analysis, yielding a per-feature histogram of filter responses for each sphere size. The measured filter responses for the DF data overlap and do not have differences in their distribution that are statistically significant (Fig. 7(a), Table 2).. The same is true for the DIC data ((Figs. 7(b) and 7(c), Table 2). The digital template-matching algorithm fared no better than digital Gabor filtering of the spheres, with no statistically significant difference in measured sphere size

noticeable for DF (Fig. 7(d)) or DIC (Fig. 7(e)), with the exception of the 0.494 μm spheres which were actually measured larger than the other two sphere sizes in DIC (Fig. 7(e)).

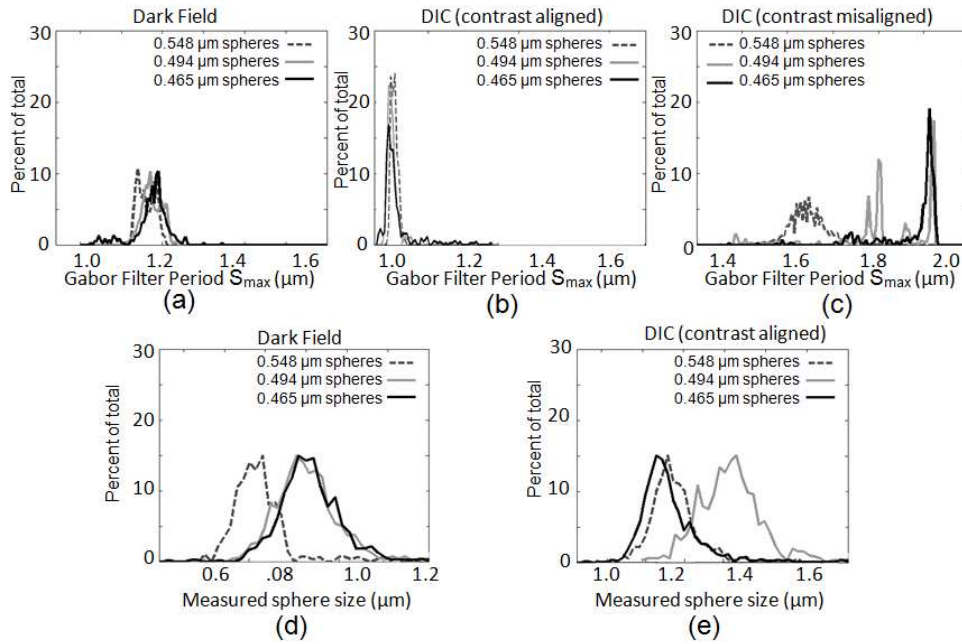


Fig. 7. Measurement of sphere size based on S_{max} values derived from digitally post-processed images. (a): Histogram derived from digital Gabor filter bank applied to dark field image. (b): Histogram derived from digital Gabor filter bank aligned to the axis of contrast applied to DIC image. (c): Histogram derived from digital Gabor filter bank misaligned with the axis of contrast applied to DIC image. (d) & (e): Sphere diameter measured using Gaussian second derivative template-matching algorithm for dark field and DIC images, respectively.

Table 2. Digital filtering response to spheres with diameter ~ 500 nm

Actual diameter (nm) *	DF		DIC (aligned with contrast)		DIC (misaligned with contrast)	
	Gabor filter period S_{max} (nm) *	Student t-test p value [†]	Gabor filter period S_{max} (nm) *	Student t-test p value [†]	Gabor filter period S_{max} (nm) *	Student t-test p value [†]
465 \pm 10	1174 \pm 42	p = 0.94	1003 \pm 94	p = 0.95	1828 \pm 218	p = 0.53
494 \pm 11	1174 \pm 24		994 \pm 24		1814 \pm 108	
548 \pm 16	1162 \pm 22	p = 0.41	1000 \pm 24	p = 0.97	1648 \pm 42	p < 0.05

* mean \pm standard deviation, [†] p value for comparison to 494nm.

4. Discussion

Optical Gabor-like filters were used to measure the change in the period of phase masks, and in the diameter of polystyrene spheres. The results demonstrate that optical processing is sensitive to a 7.5 nm change in the period of periodic phase masks (Fig. 4(b)) and is also successful at discerning finite particle sizes down to a sensitivity of 30nm as determined from polystyrene spheres ~ 500 nm in diameter (Fig. 6(c)). This sensitivity is achieved despite digital aliasing in the filtered sphere images acquired on the CCD. In contrast, and as expected, digital post-processing of aliased sphere images shows that there is insufficient

sensitivity to detect the change in sphere size using either DIC or DF contrast. Moreover, digital post-processing results are dependent on the method of imaging contrast used.

The results from digital post-processing of non-aliased periodic phase mask images indicate that high magnification is required for digital Gabor filtering to be successful (Fig. 4(c)). The confinement of the Gabor filter to two wavelengths in the image lowers the resolution of the filter in the frequency domain to such an extent that the bandwidth of the phase mask is much smaller than the bandwidth of the filter for all magnifications used here. What matters most, then, is the resolution of the image, in which oversampling in the image is the only remaining way to significantly increase sensitivity to the analysis. Therefore, because higher magnification is the only reliable way to improve accuracy of digital processing even when the object is not aliased, the dependency of digital processing on sampling is its primary limitation. This is also expected to be especially apparent for finite objects in which only one "period" of the object exists and where spatial confinement of the filter is essential.

Compared with digital post-processing, the optical processing method presented places the constraints of sensitivity solely in the sampling of the Fourier plane by the spatial light modulator; there is a much more lenient limitation on image resolution and staircasing error is eliminated by operating prior to digital sampling. Optical processing of the object's period or size characteristics prior to digitization is particularly advantageous if the final digital result is aliased and should in general allow for imaging undersampled fields of view, potentially allowing significantly greater throughput in analyzing object morphology.

In this study, we used the optimum Gabor period, S_{\max} , giving maximum response as a measure of object size at each pixel. S_{\max} was obtained after fitting a Gaussian to the pixel response curve vs. Gabor filter frequency (e.g. Figure 2(c), 6(a)). We chose the Gaussian because it is capable of extracting a local maximum (if one exists) necessary for the analysis within the data set while making few other assumptions about the remainder of the data. It is positive for all possible values of frequency, as a real signal should be as well. However, it is important to note that the Gaussian function was only used here to retrieve objectively and reproducibly the spatial frequency position of the maximum response and for this purpose resulted in good fits with good correlation values. The nature of the actual response function will in general depend on the product of the Gabor filter with the object's transform, and may not be known a priori for arbitrary samples. Better function choices could ultimately be made for specific objects where the shape of the scatter is known. This technique is similar to Optical Scatter Imaging [14] by Boustany et al., in that it measures the change in signal of the forward scatter lobe of the particle relative to scattering angle. However, by probing the angular scatter distribution of the particles finely with Gabor filters instead of implementing an optical scatter image ratio based on the intensity ratio of wide-to-narrow angle scatter as in [14], better size discrimination may be achieved. This technique has additional advantages in that it is sensitive to detecting the shape of the angular scatter profile, can be used without a scatter model, and implements optimal spatial confinement of the filtered image via Gabor filtering.

Additionally, the parameter S_{\max} intrinsically describes the object size in the correct units of length, and the data in Fig. 6 show that the relationship between S_{\max} and object size is linear for particles with diameter between $0.46\mu\text{m}$ and $1\mu\text{m}$. The linear relationship between the sphere size and Gabor period is supported by the 0.99 correlation coefficient (Fig. 6(c)) although more sphere sizes would need to be tested in similar fashion to better define the dynamic range of this relationship. In particular, the sensitivity to the size of particles which are significantly below the resolution of the optical system will decrease due to signal truncation from the numerical aperture. This begins to be apparent in the broadening of the size distributions for the smaller sphere sizes in the histograms from Fig. 6(b). The slope of this relationship is also likely to depend on the shape of the finite objects being measured. Thus, although the parameter S_{\max} is highly sensitive to changes in object size, it may not measure the absolute object size accurately in a sample consisting of objects other than spheres. Nonetheless, a linear relationship is still expected to retrieve relative changes in object size accurately in all cases. A linear relationship between S_{\max} and object size imparts

this technique with an advantage over spectroscopic methods, which require a scattering model of the spectrum in order to translate spectral changes into change in object size measured in the correct units of length [6]. The method presented here is therefore relevant for monitoring cell morphology in living samples, where the ability to detect subtle relative changes in structure without assumptions of a model may be of greater value than measuring absolute size accurately.

Future experimentation will show the effect of refractive index on this analysis; however, sphere scatter simulations show that changes in the refractive index ratio between the measured particle and the medium is not expected to change the shape of the forward scatter lobe appreciably and therefore will not change the relationship between the Gabor filter period S_{\max} and sphere diameter. Changes in the refractive index ratio will however affect the amount of signal a great deal. Biological organelles have refractive index ratios $m \sim 1.04$, while for the polystyrene spheres in polyacrylamide gel $m \sim 1.2$. The decrease from $m = 1.2$ to $m = 1.04$ corresponds to an order of magnitude loss of signal due to the reduction in scattering cross section at the lower value of m . The signal-to-noise ratio (SNR) in a shot-noise limited detection system would drop by a factor of 3 or 4 (e.g. SNR in data of Fig. 6(a)), from which signal may still be recovered, albeit with lower sensitivity. This sensitivity may be recovered immediately, by using more powerful illumination, or by examining more than one pixel at a time to average the noise out. The current fluence at the sample is $\sim 0.2 \text{ mW/mm}^2$ accounting for power losses at the diffuser and during coupling into the microscope. Thus the current laser power could be increased by a factor of 10 without damaging biological tissue, while pixel areas corresponding to $0.5 \mu\text{m} \times 0.5 \mu\text{m}$ (2×2 pixels at the current magnification) could be analyzed while remaining within the resolution of the Gabor filters used. Thus, for cases where the refractive index ratio is low (such as for cellular organelles in cytosol), accurate data collection is a signal to noise issue that can be solved either with a more powerful source of illumination, post-processing averaging, or both, and is not expected to be otherwise affected by index of refraction.

In conclusion, we have extended our previous implementation of the DMD as a spatial Fourier filter [10] by using filter banks that use additional choices of Gabor-like filter periods S to probe variations in object size. This technique does not rely on a predictive scatter model such as Mie theory, and the morphology of both finite and periodic objects can be probed with very high sensitivity at low image resolution. We expect that this technique will be useful in high-throughput morphological analysis of subcellular dynamics in greatly undersampled fields of view.

Acknowledgments

We thank Paul S. Westbrook of OFS Labs, Somerset NJ for the phase masks. This work was partially supported by Whitaker Foundation grant RG02-0682 to N. Boustany, and a Rutgers Graduate Presidential Fellowship to R. Pasternack.